RSC Advances

This is an *Accepted Manuscript*, which has been through the Royal Society of Chemistry peer review process and has been accepted for publication.

Accepted Manuscripts are published online shortly after acceptance, before technical editing, formatting and proof reading. Using this free service, authors can make their results available to the community, in citable form, before we publish the edited article. This *Accepted Manuscript* will be replaced by the edited, formatted and paginated article as soon as this is available.

You can find more information about *Accepted Manuscripts* in the Information for Authors.

Please note that technical editing may introduce minor changes to the text and/or graphics, which may alter content. The journal's standard Terms & Conditions and the Ethical guidelines still apply. In no event shall the Royal Society of Chemistry be held responsible for any errors or omissions in this *Accepted Manuscript* or any consequences arising from the use of any information it contains.

ROYAL SOCIETY OF CHEMISTRY

www.rsc.org/advances

Structural and electrical behaviour in $Bi_{14}YO_{22.5}$

M. Struzik,[1] M. Malys,[1*] M. Krynski,[1] M. Wojcik,[1] J. R. Dygas,[1] W. Wrobel,[1] F. Krok,

and I. Abrahams,[2*]

[1]Faculty of Physics, Warsaw University of Technology, ul. Koszykowa 75, 00-662 Warszawa, Poland.

[2]Materials Research Institute, Department of Chemistry and Biochemistry, School of Biological and Chemical Sciences, Queen Mary University of London, Mile End Road, London E1 4NS, U.K.

*Corresponding authors: I. Abrahams Tel. +44 207 882 3235, Email: i.abrahams@qmul.ac.uk; M. Malys, Tel. +48 22 234 8216, Email: mmalys@wp.pl

RSC Advances Accepted Manuscript

Abstract

Structure and electrical conductivity in the oxide ion conducting compound $Bi_{14}YO_{22.5}$ have been investigated by powder X-ray and neutron diffraction, a.c. impedance spectroscopy, measurements of transference number and *ab initio* molecular dynamics (MD) simulations. Phase behaviour was studied using variable temperature X-ray diffraction and differential thermal analysis. The structure at room temperature is of the β_{III} tetragonal-type, details of which are discussed, including its relationship to both β and δ phases of Bi_2O_3. $Bi_{14}YO_{22.5}$ undergoes a reversible phase transition to a cubic δ-Bi_2O_3 type phase at high temperatures. This phase exhibits very high electrical conductivity, with transference numbers indicating that this conductivity is almost purely ionic in nature. MD simulations confirm 3-dimensional oxide ion transport in the β_{III}-phase.

Keywords: Bismuth oxide, bismuth yttrium oxide, oxide ion conductors; defect structure; neutron diffraction; X-ray diffraction; ac impedance spectroscopy, ab initio DFT, MD simulations.

RSC Advances Accepted Manuscript

1. Introduction

There is much current interest in fast oxide ion conducting solids for use as solid electrolytes in various electrochemical devices, such as fuel cells, oxygen pumps, sensors, *etc*. Much of this research is focused on developing materials suitable for intermediate temperature (*ca*. 500 °C to *ca*.700 °C) devices. The highest known oxide ion conductivity in a solid is seen in bismuth oxide. This oxide shows complex polymorphism, with two stable polymorphs, α and δ, observed on heating and two metastable polymorphs, β and γ, obtainable depending on cooling conditions. The high temperature δ-phase possesses high oxide ion conductivity, with values in the order of 1 S cm^{-1} at temperatures above *ca*. 730 °C.[1] Partial substitution of bismuth by a variety of cations can lead to stabilization of the δ-phase or closely related ordered fluorite phases at room temperature.[2-7]

At relatively low levels of substitution of bismuth (*ca*. 0.05 mol%), β or γ (sillenite) phases are often observed. Above this level of substitution, a variety of fluorite based phases can be obtained, depending on the dopant and level of substitution. Recently, there has been interest in phases with a Bi:M ratio of 14:1 (6.67 mol% substitution), such as $Bi_{14}ReO_{24.5}$ [8,9] and $Bi_{14}MO_{24}$ (where M = W, Mo, Cr) [10]. $Bi_{14}ReO_{24.5}$ exhibits exceptionally high conductivity at intermediate temperatures, in the order of 10^{-3} S cm^{-1} at 300°C.[8,9]

The $(Bi_{1-x}Y_x)_2O_3$ system has been reviewed by Sammes *et al*.[5] At bismuth rich compositions, around the 14:1 Bi:Y ratio, a tetragonal phase is observed, which forms part of a solid solution range extending from *ca*. 5.8 to *ca*. 8.1%.[11] However, it has been argued by Watanabe [12] that the observed tetragonal solid solution is in fact metastable. Using an alternative phase diagram, he argued that the lowest *x*-value room temperature stable phase in this system is the end member of a solid solution ranging from $x = 0.215$ to $x = 0.24$, with compositions at lower *x*-values possessing only mixtures of this phase and α-Bi_2O_3 as the stable phases.

We have previously studied δ-phase compositions around $x = 0.25$ in the $(Bi_{1-x}Y_x)_2O_3$ system, which show high levels of conductivity [13,14] and revealed details of the vacancy ordering, using total neutron scattering analysis.[15] Ab initio modelling of the $x = 0.25$ composition reveals that yttrium acts as a trap for mobile oxide ions, effectively lowering ionic conductivity compared to the parent δ-Bi_2O_3.[16] In the present study we examine a more bismuth rich composition in the

RSC Advances Accepted Manuscript

$(Bi_{1-x}Y_x)_2O_3$ system at the 14:1 Bi:Y ratio (x = 0.067), which exhibits a tetragonal structure at room temperature and a cubic fluorite phase at high temperatures.[12] Here details of the structure and electrical conductivity of this composition have been studied in detail using X-ray and neutron powder diffraction, in combination with a.c. impedance spectroscopy, differential thermal analysis (DTA) and measurements of transference number. These results are compared with those from *ab initio* molecular dynamics calculations.

2. Experimental

2.1 Sample preparations

The title compound, $Bi_{14}YO_{22.5}$ was prepared using stoichiometric amounts of Bi_2O_3 (Aldrich, 99.99%) and Y_2O_3 (Aldrich, 99.95%). The starting mixture was ground in ethanol using a planetary ball mill for *ca*. 24 h. The dried mixture was heated initially at 750 °C for 24 h, then cooled, reground and pelletized. Pellets were pressed isostatically at a pressure of 400 MPa, then sintered at 800 °C for 24 h, before cooling in air to room temperature over a period of approximately 12 h.

2.2 Electrical measurements

Electrical parameters were determined by a.c. impedance spectroscopy using a fully automated Solartron 1255/1286 system, in the frequency range 1 Hz to 5×10^5 Hz (18 frequencies per decade). Samples for impedance measurements were rectangular blocks (*ca*. $6 \times 2 \times 3$ mm^3) cut from sintered pellets using a diamond saw. Platinum electrodes were sputtered by cathodic discharge on the two smallest flat polished parallel faces of the blocks. Impedance spectra were recorded during heating and cooling ramps between *ca*. 300 °C and *ca*. 800 °C, at stabilized temperatures. Drift of impedance was monitored during measurement using an algorithm described earlier [17] and controlled to be within 2%.

The ionic and electronic contributions to the total conductivity were measured using a modified EMF method, with an external adjustable voltage source in the concentration cell

RSC Advances Accepted Manuscript

$O_2(pO_2 = 1.01 \times 10^5$ Pa): Pt | oxide | Pt : O_2 ($pO_2 = 0.2095 \times 10^5$ Pa), as described in detail elsewhere.[18] Measurements were performed on cooling between *ca*. 780 °C and 430 °C at stabilized temperatures. Samples were prepared as sintered pellets of 14 mm diameter and *ca*. 2 mm thickness. The Pt electrode had a diameter of 10.7 mm.

2.3 Differential Thermal Analysis

Differential thermal analysis (DTA) was carried out using a TA Instruments Q600 scanning differential thermal analyser. Approximately 50 mg of powdered sample in an alumina crucible was monitored over heating and cooling cycles, between ambient temperature and 900 °C at a heating/cooling rate of 20 °C min^{-1} in flowing air.

2.4 Diffraction

X-ray powder diffraction data were collected on a Philips X'Pert Pro X-ray diffractometer using Ni filtered Cu-Kα radiation (λ_1 = 1.54056 Å and λ_2 = 1.54439 Å) in flat plate θ/θ geometry with an X'Celerator detector. Calibration was carried out with an external LaB_6 standard. Data were collected at selected temperatures in the range ambient to 850 °C, using an Anton-Paar HTK 1200 camera. Data at room temperature and at 800 °C were collected over the 2θ range 5-105°, in steps of 0.033°, with a scan time of 250 s per step. For intermediate temperatures, shorter scans were performed with a scan time of 25 s per step.

Powder neutron diffraction data were collected on the Polaris diffractometer at the ISIS Facility, Rutherford Appleton Laboratory. Data collected on back-scattering and low-angle detectors were used in subsequent refinements, covering the respective time of flight ranges 1.0 to 20 and 0.5 to 20 ms. The sample was contained in a cylindrical 11 mm diameter vanadium can located in front of the back-scattering detectors. Data were collected at room temperature for *ca*. 200 μA h.

Structure refinement was carried out by Rietveld whole profile fitting using the GSAS suite of programs.[19] For the room temperature analysis, a combined X-ray and neutron approach

RSC Advances Accepted Manuscript

was adopted. For the high temperature phase, a simple cubic fluorite model in space group *Fm*-3*m* was used for refinements, as previously described.[13] For the low temperature structure, initial refinements were based on the structure of β-Bi_2O_3 [20,21] in space group *P*-42$_1$*c* (no. 114 [22]). Difference Fourier maps were used to locate interstitial oxide ion scattering density. It was found that the structure exhibited considerable positional disorder with respect to the structure of β-Bi_2O_3. The systematic absences for space group *P*-42$_1$*c* are in fact a subset of those for *P*4$_2$/*nmc*, and therefore a satisfactory refinement can be obtained in the lower symmetry space group, even when the true symmetry is higher. However, close inspection of the diffraction data reveal that the systematic absences are consistent with the higher symmetry space group, showing absence of Bragg peaks of the type *hk*0, when $h + k = 2n + 1$ (Fig. 1). We have previously reported the structure of β_{III}-$Bi_{1.85}Zr_{0.15}O_{3.075}$ [23] in space group *P*4$_2$/*nmc* (no. 137, origin choice 2 [22]). This model is also consistent with that proposed for $Bi_7Y_{0.5}O_{25}$,[24] but exhibits greater positional disorder. Refinement of the β_{III}-model resulted in an excellent fit to the data for $Bi_{14}YO_{22.5}$ at room temperature and the structure presented here corresponds to this model. The extent of Y substitution in the present system is low and therefore Bi and Y atom parameters were tied to a single site. Anisotropic displacement parameters were refined for all atoms. A large U_{33} parameter on O(3) indicated that the site was split and in the final refinements this was placed on an 8*g* site. Oxide ion site occupancies were initially allowed to vary. The occupancies for O(1) and O(3) were found to be correlated with the amount of yttrium in the system and in the final refinements these were fixed according to stoichiometry. Crystal and refinement parameters for $Bi_{14}YO_{22.5}$ at room temperature are presented in Table 1.

2.5 DFT calculations

Density functional theory (DFT) calculations were carried out within a 2 × 2 × 1 supercell (160 ions in total) of β_{III}-$Bi_{14}YO_{22.5}$ using the Vienna Ab-initio Simulation Package (VASP) and a plane wave basis set.[25-28] The exchange-correlation function was treated within the generalized gradient approximation of Perdew–Burke–Ernzerhof [29] and the electron–ion interactions were described by the full potential projector augmented wave method,[30] with 5, 6 and 11 valence electrons for Bi, O and Y respectively (including 4*s* and 4*p* electrons for the latter). Forces were

RSC Advances Accepted Manuscript

calculated according to the Hellmann–Feynman theorem [31,32] and the kinetic energy was controlled by means of the Nose–Hoover thermostat.[33,34] The plane wave cutoff energy was 430 eV for all calculations. The sampling of the Brillouin zone was performed using the Monkhorst–Pack scheme [35] at the gamma point. All calculations were performed under periodic boundary conditions. The MD simulations were performed from initially relaxed structures. The global break point for the electronic loop was set to 10^{-5} eV/cell. The initial structural model was based on the results from the diffraction analysis. Bismuth and yttrium atoms were distributed randomly over the cation sites in the supercell, while oxygen atoms were distributed quasi randomly over the three types of anion site according to the site occupancies in the crystallographic model. The MD simulations were carried out at 850 °C, over a total of 40 ps in steps of 5 fs. Three parallel runs were performed to yield sufficient statistical quality. To minimize the influence of initial thermodynamic relaxation of the system, the data corresponding to the first 5 ps were not taken into account for further analysis. The simulation temperature of 850 °C, although above the existence range of the β_{III}-phase (see discussion), was chosen to ensure sufficient oxide ion movement within a reasonable simulation time.

To capture the oxide ion jump trajectories, high frequency oscillations of the oxide ions were excluded from calculations using a low pass Chebyshev filter. The cutoff frequency for the Chebyshev filter was determined based on the Fourier analysis of the ionic trajectories. For the frequencies above 5×10^{12} Hz, only thermal vibrations are observed. Energy distribution landscapes were derived from ionic density maps assuming a Boltzmann distribution.

Structural graphics were prepared using ORTEP-3 for Windows [36] and VESTA [37].

3. Results and Discussion

3.1 Structure of β_{III}-$Bi_{14}YO_{22.5}$

Fitted diffraction profiles from the Rietveld analysis of β_{III}-$Bi_{14}YO_{22.5}$ at room temperature are shown in Fig. 2, with the refined structural parameters given in Table 2 and significant contact distances in Table 3. The structure of β_{III}-$Bi_{14}YO_{22.5}$ is closely related to that of Pb_2F_2O.[38] An idealised model of β_{III}-$Bi_{14}YO_{22.5}$ (containing no structural disorder) consists interconnected

RSC Advances Accepted Manuscript

Bi_4O_4 rings, with bismuth in an essentially trigonal pyramidal geometry, forming a corrugated layered structure, with layers stacked parallel to the *c*-axis (Fig. 3). The Bi_4O_4 rings in adjacent layers are aligned such that they form a channel structure, with channels running parallel to the *c*-axis .

The structure of β_{III}-$Bi_{14}YO_{22.5}$ may be thought of as lying between those of β-Bi_2O_3 and δ-Bi_2O_3 (Fig. 4). The structure of β-Bi_2O_3,[21] consists of a near cubic close packed array of bismuth cations, with O^{2-} anions distributed in ¾ of the tetrahedral cavities. The vacant tetrahedral cavities are ordered to yield channels perpendicular to the *c*-axis. The main difference between the structures of the β and δ phases of Bi_2O_3 lies in the vacancy ordering. In the latter case, vacancies are disordered over all the tetrahedral cavities on the crystallographic scale. Additionally, the cations in β-Bi_2O_3 are arranged in a slightly corrugated fashion above and below the *x*-*y* plane, while in the structure of δ-Bi_2O_3, the cations lie within the corresponding planes, as clearly evident in Fig. 3. In the case of the β_{III}-phase, the cation distribution shows the ideal planarity of the δ-phase, but the anion distribution more closely resembles that in the β-phase. The O(1) and O(2) sites in β_{III}-$Bi_{14}YO_{22.5}$ lie close to the corresponding sites in β-Bi_2O_3. However, the O(3) site in the β_{III}-phase corresponds to a site in the vacant channels of the β-phase and hence, in this respect, the anion distribution of the β_{III}-phase approaches that of the δ-phase. The O(1) site shows positional disorder compared to the corresponding position in β-Bi_2O_3. Since the shortest O(1)..O(1) contact distance is only 0.379 Å, a maximum occupancy of 0.5 is possible for this site. The initial refinements indicated that the occupancy of the O(1) site was significantly lower than this maximum value, with the total number of oxide ions on this site approximately equal to the amount of bismuth in the structure.

In β_{III}-$Bi_{14}YO_{22.5}$, the bismuth coordination is asymmetric, reflecting stereochemical activity of the Bi $6s^2$ lone pair of electrons, with three short Bi-O contacts of 2.11 to 2.25 Å and longer Bi-O contacts of 2.59 to 2.84 Å (the number of contacts takes into account the disorder on the O(1) site, which prevents simultaneous occupancy of neighbouring sites). These longer contacts may be considered to be non-bonding interactions, resulting in an essentially trigonal pyramidal coordination for Bi (Fig. 5a). The weighted average O-Bi-O angle within the trigonal pyramid is 85.7° for the configuration shown in Fig. 5a, which is again consistent with

RSC Advances Accepted Manuscript

stereochemical activity of the Bi $6s^2$ lone pair of electrons. Based on geometrical considerations only, the alignment of the Bi $6s^2$ lone pair is such that it points towards the nominally empty channel (nominally empty, since O(3) is located in the channel), as previously described in the β_{III}-$Bi_{1.85}Zr_{0.15}O_{3.075}$ system.[23] The O(3) site occupancy initially refined close to double that of the yttrium occupancy of the Bi/Y 8*g* site and taking into account the multiplicities of these two sites this gave an approximate 1:1 ratio for Y:O(3). The absence of atoms in a position corresponding to O(3) in the undoped system, β-Bi_2O_3 and the 1:1 Y:O(3) ratio, suggest that oxide ions on the O(3) site are exclusively associated with the Y^{3+} cation and allow it to adopt a more characteristic distorted octahedral coordination geometry involving O(1), O(2) and O(3) ions (Fig. 5b). The average Y-O bond length is 2.31 Å, which is slightly longer than the average value of 2.27 Å observed in Y_2O_3.[39] Bond valence sums calculated using the parameters of Brese and O'Keeffe [40] for Bi^{3+} and Y^{3+} were 3.08 and 3.03, respectively, for the proposed coordination geometries in Fig. 5.

The geometrical position of the bismuth lone pairs is critical in determining the nature of the ionic conduction mechanism in this compound. In order to examine details of the nature of the interactions between bismuth and the surrounding oxygen atoms, *ab initio* calculations of the valence electron distribution in β_{III}-$Bi_{14}YO_{22.5}$ were carried out. Fig. 6a shows an iso-surface plot of valence electron density of a representative bismuth atom from these calculations. The figure clearly shows significant polarization of electron density between bismuth and the three closest oxygen atoms, indicative of a significant degree of covalency in these interactions. The next nearest oxygen atoms show no obvious polarization of electron density in the direction of the bismuth atom, consistent with these interactions being much weaker in bonding character. The three bonded atoms are arranged in a trigonal pyramidal coordination with bismuth, with the lone pair on bismuth pointing out of the pyramid apex. The results therefore agree with the proposed directionality of the bismuth lone pair based on the geometrical considerations above. Fig. 7 shows the valence electron density around a nominally empty channel in β_{III}-$Bi_{14}YO_{22.5}$ and confirms that the lone pairs on bismuth point into the channel as previously proposed in the structure of β_{III}-$Bi_{1.85}Zr_{0.15}O_{3.075}$.[23] An iso-surface plot of valence electron density around a representative yttrium atom is shown in Fig. 6b. The figure reveals six oxygen atoms in the yttrium coordination sphere, confirming the coordination derived from the crystallographic

RSC Advances Accepted Manuscript

analysis. Interestingly, only one of the oxygen atoms shows significant polarization of electron density in the direction of the yttrium atom. This suggests that the majority of yttrium-oxygen contacts are ionic in nature.

3.2 Thermal and electrical behaviour of $Bi_{14}YO_{22.5}$

The DTA thermogram for $Bi_{14}YO_{22.5}$ is shown in Fig. 8. On heating, a single endothermic event is observed with an onset temperature of 639 °C, while on cooling the corresponding endotherm occurs at 551 °C. No melting endotherm is observed on heating in the temperature range studied. The thermal evolution of the X-ray diffraction pattern of the title compound is shown in Fig. 9. These data confirm a direct transition from the tetragonal β_{III}-phase to a cubic fcc phase between 600 and 650 °C on heating, with some residual tetragonal phase evident in the diffraction pattern at 650 °C. The reverse transition occurs between 600 and 550 °C on cooling. In order to analyse the structure volume expansion as a function of temperature, it is helpful to define an equivalent fluorite cell volume (V_f):

$$V_f = \frac{V_t}{2} \qquad (1)$$

where V_t is the unit cell volume of the tetragonal phase. Fig. 10 shows the thermal variation of V_f. On heating, a linear expansion of the lattice is observed up to 600 °C, with a large jump in volume between 600 and 650 °C, associated with the tetragonal to cubic phase transition. The reverse transition on cooling is shifted to 550 °C. The large difference in V_f between the tetragonal and cubic phases is associated with significant disorder in the latter phase.[15] There is a small difference in cell volume of the tetragonal phase between heating and cooling runs, which might indicate differing degrees of disorder, with the slow cooled sample in the X-ray experiment exhibiting some structural relaxation. This is not an unusual phenomenon, although it is typically associated with differing degrees of oxidation of the dopant cations.[41]

Fig. 11 shows the Arrhenius plot of total conductivity for the title compound on heating and cooling. Two linear regions are observed, one at low temperatures and a second of lower activation energy at high temperatures, with a significant jump in conductivity between the low

RSC Advances Accepted Manuscript

and high temperature regions. There is thermal hysteresis associated with the transition, which occurs at around 650 °C on heating and *ca*. 550 °C on cooling, in good agreement with the results from DTA and X-ray measurements. The characteristic values of conductivity at 300 °C (σ_{300}) and at 800 °C (σ_{800}) are 1.06(1) × 10^{-5} S cm^{-1} and 1.83(7) S cm^{-1}, respectively. The corresponding activation energies for the low (ΔE_{LT}) and high (ΔE_{HT}) temperature regions are 0.96(1) eV and 0.64(4) eV, respectively. These values confirm very high conductivity for the cubic fluorite phase.

Fig. 12 shows the thermal variation of ionic transference number for $Bi_{14}YO_{22.5}$ on cooling. The plot reflects the cubic to tetragonal phase transition seen in this system, with a transition between *ca*. 650 and 600 °C. The transition occurs at around the same temperature as seen in heating measurements using other techniques and reflects the fact that very long equilibration times are used in the transference number measurements. Both tetragonal and cubic phases show predominantly ionic conductivity over the measured temperature range, with the tetragonal phase exhibiting a transference number of around 0.8 and the cubic phase around 0.95 for oxide ion conduction.

We have previously proposed an oxide ion transport mechanism for the β_{III}-phase in the bismuth zirconate system,[23] involving oxide ion hopping along the *c*-axis channels, facilitated by the positioning of the bismuth lone electron pairs. It is possible to use the results from the DFT calculations to derive a 3-dimensional map of energy distribution, which allows for the identification of energetically favourable pathways for oxide ion migration. An energy distribution landscape was derived from the ionic density map assuming a Boltzmann distribution of ion positions:[16,42]

$$N_x = N_0 \cdot e^{-\frac{\Delta E}{kT}} \qquad (2)$$

where N_x represents the number of times that oxide ions were present at position x, N_0 is the number of times that oxide ions were present at the point of highest ionic density, k is the Boltzmann constant, T is the temperature and ΔE is the energy difference between position x and the point of highest ionic density.

RSC Advances Accepted Manuscript

Energy distribution landscapes for vacant and filled channels in the structure of β_{III}-$Bi_{14}YO_{22.5}$ are shown in Fig. 13. The energy barriers at the saddle points for conduction along the channels are lower in the empty channels compared to those in the filled channels, with average values of 0.39 and 0.44 eV, respectively. Traces of oxide ion movements over the total simulation time (Fig. 14) show that oxide ion jumps occur not only through the *c*-axis channels (in the *z*-direction), but also between channels in the *x*-*y* plane. These results suggest that ion conduction in β_{III}-$Bi_{14}YO_{22.5}$ is in fact 3-dimensional in character and is similar to that in δ-Bi_2O_3. The level of ionic conductivity in the β_{III}-phase is relatively low compared to that in the δ-phase observed at high temperatures. This can be attributed to the reduced mobility of oxide ions at lower temperatures. Interestingly, at higher levels of substitution ($x = 0.25$) in the $(Bi_{1-x}Y_x)_2O_3$ system, where the δ-phase is readily preserved to room temperature, low temperature values of ionic conductivity are quite similar ($\sigma_{300} = 3.7 \times 10^{-5}$ S cm^{-1} in Bi_3YO_6) to those in the present study, but a higher value of the low temperature activation energy ((ΔE_{LT} = 1.19 eV) [15] is observed in the δ-phase.

4. Conclusions

$Bi_{14}YO_{22.5}$ adopts a β_{III}-type tetragonal structure at room temperature, which is closely related to that of β-Bi_2O_3. Crystal structure analysis and *ab initio* calculations confirm that bismuth exhibits a trigonal pyramidal bonding coordination with oxygen atoms, with stereochemical activity of the bismuth $6s^2$ lone pairs, which point into the nominally vacant channels running parallel to the *c*-axis. Yttrium atoms are proposed to exhibit a distorted octahedral coordination environment, with the majority of close Y-O interactions predominantly ionic in nature. $Bi_{14}YO_{22.5}$ shows polymorphism, with a cubic δ-Bi_2O_3 type phase occurring at elevated temperatures. Thermal hysteresis is evident in the tetragonal ↔ cubic phase transition, with the transition on cooling occurring at almost 100 °C lower than on heating. No evidence was seen in this study for instability of the tetragonal or cubic phases under the experimental conditions used. Cubic δ-$Bi_{14}YO_{22.5}$ exhibits very high electrical conductivity at 800 °C and is confirmed as being almost a pure ionic conductor. MD simulations confirm the conduction mechanism to be 3-dimensional in character, similar to that observed in the δ-phase.

RSC Advances Accepted Manuscript

Acknowledgements

We are grateful to Dr. S. Hull at the Rutherford Appleton Laboratory, for his help in neutron data collection and the STFC ISIS facility for beam time. IA gratefully acknowledges the Centre of Advanced Studies, Warsaw University of Technology for a visiting professorship. We gratefully acknowledge the National Science Centre Poland for project grant numbers 2012/05/E/ST3/02767 and 2013/09/N/ST3/04326.

References

1. T. Takahashi, H. Iwahara and Y. Nagaj, *J. Appl. Electrochem*., 1972, **2**, 97.

2. G. Mairesse, in Fast Ion Transport in Solids, B. Scrosati, A. Magistris, C.M. Mari, G. Mariotto (Eds.), Kluwer Academic Publishers, Dordrecht, 1993, p271.

3. J.C. Boivin and G. Mairesse, *Chem. Mater*., 1998, **10**, 2870.

4. P. Shuk, H.D. Wiemhöfer, U. Guth, W. Göpel and M. Greenblatt, *Solid State Ionics*, 1996, **89**, 179.

5. N.M. Sammes, G.A. Tompsett, H. Näfe and F. Aldinger, *J. Eur. Ceram. Soc*., 1999, **19**, 1801.

6. A.M. Azad, S. Larose and S.A. Akbar, *J. Mater. Sci.,* 1994, **29**, 4135.

7. J.B. Goodenough, A. Manthiram, M. Paranthaman and Y.S. Zhen, *Mater. Sci. Eng*., 1992, **B12**, 357.

8. T.E. Crumpton, J.F.W. Mosselmans and C. Greaves, *J. Mater. Chem*., 2005, **15**, 164.

9. R. Punn, A. M. Feteira, D.C. Sinclair and C. Greaves, *J. Am. Chem. Soc*., 2006, **128**, 15386.

10. T.E. Crumpton, M.G. Francesconi and C. Greaves, *J. Solid State Chem*., 2003, **175**, 197.

11. R.K. Datta and J.P. Meehan, *Z. Anorg. Allgem. Chem*., 1971, **383**, 328.

12. A. Watanabe, *Solid State Ionics*, 1996, **86-88**, 1427.

RSC Advances Accepted Manuscript

13. I. Abrahams, A. Kozanecka-Szmigiel, F. Krok, W. Wrobel, S.C.M. Chan and J.R. Dygas, *Solid State Ionics*, 2006, **177**, 1761.

14. F. Krok, I. Abrahams, M. Holdynski, A. Kozanecka-Szmigiel, M. Malys, M. Struzik, X. Liu and J.R. Dygas, *Solid State Ionics*, 2008, **179**, 975.

15. I. Abrahams, X. Liu, S. Hull, S.T. Norberg, F. Krok, A. Kozanecka-Szmigiel, M.S. Islam and S.J. Stokes, *Chem. Mater*., 2010, **22**, 4435.

16. M. Krynski, W. Wrobel, C.E. Mohn, J. R. Dygas, M.Malys, F. Krok and I. Abrahams, *Solid State Ionics*, 2014, **264**, 49.

17. J.R. Dygas, P. Kurek and M.W. Breiter, *Electrochim. Acta,* 1995, **40**, 1545.

18. M. Malys, J.R. Dygas, M. Holdynski, A. Borowska-Centkowska, W. Wrobel and M. Marzantowicz, *Solid State Ionics*, 2012, **22**, 493.

19. A. C. Larson and R. B. Von Dreele, *Los Alamos National Laboratory Report*, 1987 LAUR-86-748.

20. S.K. Blower and C. Greaves, *Acta Crystallogr*., 1988, **C44**, 587.

21. S. Hull, S.T. Norberg, M.G. Tucker, S.G. Eriksson, C.E. Mohn and S.Stolen, *Dalton Trans.* 2009, 8737.

22. International Tables for Crystallography, Volume A Space Group Symmetry, Ed. T. Hahn, International Union of Crystallography, Kluwer Academic Publishers: Dordrecht, The Netherlands, 1992.

23. I. Abrahams, A.J. Bush, S.C.M. Chan, F. Krok and W. Wrobel, *J. Mater. Chem*., 2001, **11**, 1715.

24. J. Ducke, M. Troemel, D. Hohlwein and D Kizler, *Acta Crystallogr.,* 1996, **C52**, 1329.

25. G. Kresse and J. Hafner, *Phys. Rev. B*, 1998, **47**, 558.

26. G. Kresse and J. Hafner, *Phys. Rev. B,* 1994, **49**, 14251.

RSC Advances Accepted Manuscript

27. G. Kresse and J. Furthmüller, *Phys. Rev. B*, 1996, **54**, 11169.

28. G. Kresse and J. Furthmüller, *Comp. Mater. Sci.,* 1996, **6**, 15.

29. J. Perdew, K. Burke and M. Ernzerhof, *Phys. Rev. Lett*., 1996, **77**, 3865.

30. G. Kresse and J. Joubert, *Phys. Rev. B*, 1999, **59**, 1758.

31. H. Hellmann and F. Deuticke, "*Einführung in die Quantenchemie*", Leipzig, **1937**.

32. R. Feynman, *Phys. Rev.,* 1939, **56**, 340.

33. S. Nosé, *J. Chem. Phys.,* 1984, **81**, 511.

34. W. Hoover, *Phys. Rev. A,* 1985, **31**, 1695.

35. H. J. Monkhorst and J.D. Pack, *Phys. Rev. B*, 1976, **13**, 5188.

36. L. Farrugia, *J. Appl. Cryst.,* 1997, **30**, 565.

37. K. Momma and F. Izumi, *J. Appl. Crystallogr.,* 2011, **44**, 1272.

38. B. Aurivillius, *Chem. Scr.,* 1976, **10**, 156.

39. M.G. Paton and E.N. Maslen, *Acta Crystallogr*., 1965, **19**, 307.

40. N.E. Brese and M. O'Keeffe, Acta Crystallogr., 1991, **B47**, 192.

41. M. Holdynski, M. Sintyureva, X. Liu, W.Wrobel, J.R. Dygas, M. Pisarek, R.M. Nix, F. Krok and I. Abrahams, *J. Phys.: Condens. Matter*, 2012, **24**, 045904.

42. A. Kushima, B. Yildiz, *J. Mater. Chem.* **20** (2010) 4809.

RSC Advances Accepted Manuscript

Table 1 Crystal and refinement parameters for $Bi_{14}YO_{22.5}$ at room temperature

Chemical formula	$Bi_{14}YO_{22.5}$
Formula weight	3374.62 g mol^{-1}
Crystal system	Tetragonal
Space group	$P4_2/nmc$
Unit cell dimension	a = 7.75622(3) Å, c = 5.63625(3) Å
Volume	339.071(3) $Å^3$
Z	0.533
Density (calculated)	8.814 g cm^{-3}
R-factors[a]	(a) Neutron backscattering R_{wp} = 0.0111, R_p = 0.0230, R_{ex} = 0.0062, R_F2 = 0.0351 (b) Neutron low angle R_{wp} = 0.0281, R_p = 0.0325, R_{ex} = 0.0220, R_F2 = 0.0840 (c) X-ray R_{wp} = 0.0405, R_p = 0.0251, R_{ex} = 0.0170, R_F2 = 0.2044 (d) Overall R_{wp} = 0.0174, R_p = 0.0252, χ^2 = 3.151
Total no. of variables	140
No of profile points used	3949 (neutron backscattering) 5139 (neutron low angle) 2842(X-ray)
No. of reflections	1237 (neutron back-scattering) 1023 (neutron low-angle) 232 (X-ray)

[a]For definition of R-factors see[19]

RSC Advances Accepted Manuscript

Table 2 Refined structural parameters for $Bi_{14}YO_{22.5}$ at room temperature

Atom	Wyc.	*x*	*y*	*z*	Occ.
Bi/Y	8*g*	0.25	0.00572(5)	0.48660(6)	0.933/0.067
O(1)	16*h*	0.5428(4)	0.0590(4)	0.2797(5)	0.467
O(2)	4*d*	0.25	0.25	0.6496(1)	1
O(3)	4*c*	0.25	0.75	0.3110(9)	0.133

Anisotropic thermal parameters ($Å^2$)

Atom	U_{11}	U_{22}	U_{33}	U_{12}	U_{13}	U_{23}
Bi/Y	0.0308(2)	0.0102(2)	0.0204(2)	0	0	-0.0067(1)
O(1)	0.0176(5)	0.0405(11)	0.0157(11)	0.0052(5)	-0.0030(6)	0.0166(7)
O(2)	0.0346(4)	0.0124(4)	0.0204(4)	0	0	0
O(3)	0.043(5)	0.076(7)	0.016(4)	0	0	0

Table 3 Bond lengths (Å) and angles (°) for $Bi_{14}YO_{22.5}$ at room temperature

Bi/Y-O(1)	2.138(4) × 2		O(1)-Bi/Y-O(1)	97.49(9)
Bi/Y-O(1)’	2.250(4) × 2		O(1)-Bi/Y-O(1)’	90.19(3)
Bi/Y-O(2)	2.1057(5)		O(1)-Bi/Y-O(2)	86.70(7)
Bi/Y-O(3)	2.217(2)		O(1)-Bi/Y-O(3)	93.72(10)
Bi/Y…O(1)’’	2.842(2) × 2		O(1)’-Bi/Y-O(1)’	82.33(9)
Bi/Y…O(1)’’’	2.586(2) × 2		O(1)’-Bi/Y-O(2)	80.22(7)
Bi/Y..O(2)’	2.6829(6)		O(1)’-Bi/Y-O(3)	100.26(12)
Bi/Y..O(3)’	2.598(3)		O(2)-Bi/Y-O(3)	179.354(1)

RSC Advances Accepted Manuscript

Figure captions

Fig. 1. Detail of fit to neutron low-angle data in space group $P\text{-}42_1c$, showing systematic absence of $hk0$ peaks when $h + k = 2n + 1$. Position of the absent 210 peak is marked by an asterisk.

Fig. 2. Fitted diffraction profiles for $Bi_{14}YO_{22.5}$ at room temperature showing observed (+ signs) calculated (line) and difference (lower) profiles. Reflection positions are indicated by markers; (a) neutron back-scattering, (b) neutron low-angle and (c) X-ray fits are shown.

Fig. 3. Idealised structure of β_{III}-$Bi_{14}YO_{22.5}$ (excluding disorder for clarity) showing corrugated layers of bismuth oxide. Cations are indicated by violet spheres and oxide ions by red spheres. The *c*-axis direction is indicated.

Fig.4. Comparison of structures for β-Bi_2O_3, β_{III}-$Bi_{14}YO_{22.5}$ and idealized structure of δ-Bi_2O_3. Cations are indicated by violet spheres, with oxide ions by red spheres and disorder indicated by partial filling of spheres.

Fig. 5. Proposed coordination geometries for (a) bismuth atoms; (b) yttrium atoms. Contact distances (Å) are shown with non-bonding interactions indicated by dashed lines. Thermal ellipsoids are drawn at 50% probability.

Fig. 6. Iso-surface plots of valence electron density from *ab initio* calculation of β_{III}-$Bi_{14}YO_{22.5}$ showing (a) bismuth environment and (b) yttrium environment. Positions of bismuth, yttrium and oxygen atoms are indicated by blue, violet and red spheres, respectively.

Fig. 7. Iso-surface plot derived from *ab initio* calculations showing valence electron density around vacant channel in β_{III}-$Bi_{14}YO_{22.5}$. Positions of bismuth and oxygen atoms are indicated by blue and red spheres, respectively. The bismuth lone electron pairs are marked.

Fig. 8. DTA Thermogram for $Bi_{14}YO_{22.5}$. Heating and cooling runs are indicated by arrows.

Fig. 9. X-ray diffraction patterns for $Bi_{14}YO_{22.5}$ on heating and cooling.

Fig. 10. Thermal evolution of equivalent fluorite volume, V_f, in $Bi_{14}YO_{22.5}$ on heating (open symbols) and cooling (filled symbols).

RSC Advances Accepted Manuscript

Fig. 11. Arrhenius plot of total electrical conductivity for $Bi_{14}YO_{22.5}$ on successive heating (open symbols) and cooling (closed symbols) runs.

Fig. 12. Thermal variation of ionic transference number in $Bi_{14}YO_{22.5}$.

Fig. 13. Energy distribution landscapes in β_{III}-$Bi_{14}YO_{22.5}$, showing sections through (a) an empty channel and (b) a filled channel. Scales are given in eV.

Fig. 14. Individual oxide ion trajectories (marked by different colours) projected onto (a) *x*-*y* and (b) *x*-*z* planes in β_{III}-$Bi_{14}YO_{22.5}$.

RSC Advances Accepted Manuscript

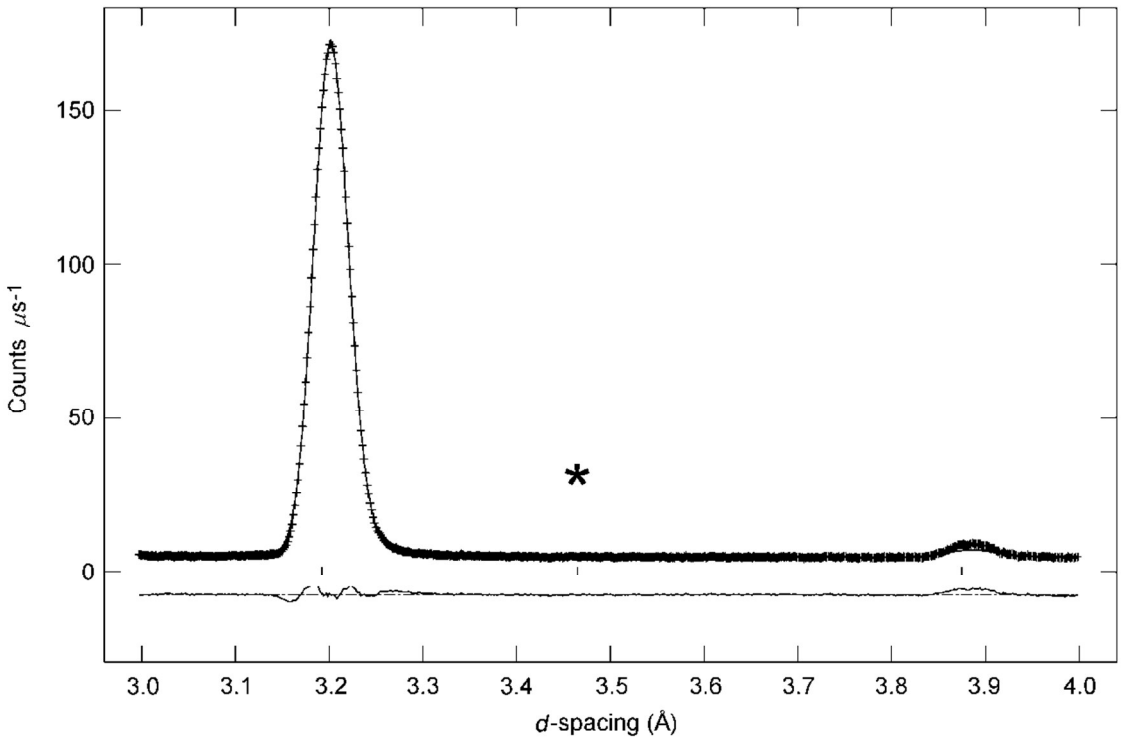

Fig. 1. Detail of fit to neutron low-angle data in space group $P\text{-}42_1c$, showing systematic absence of $hk0$ peaks when $h + k = 2n + 1$. Position of the absent 210 peak is marked by an asterisk.

RSC Advances Accepted Manuscript

(a)

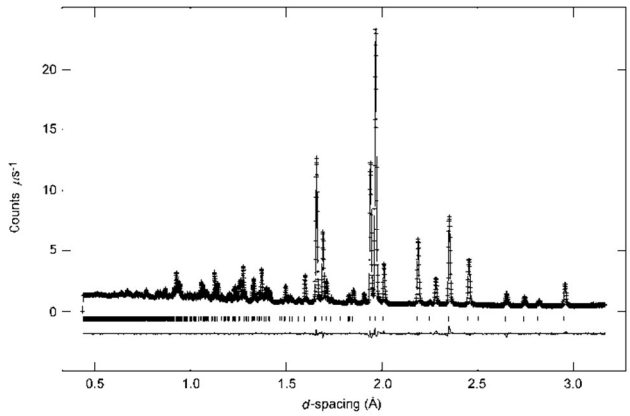

(b)

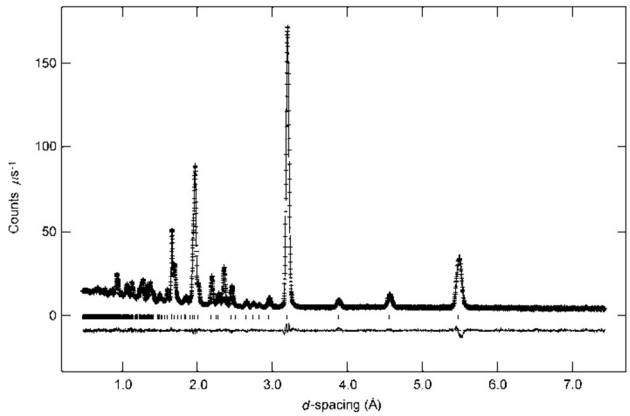

(c)

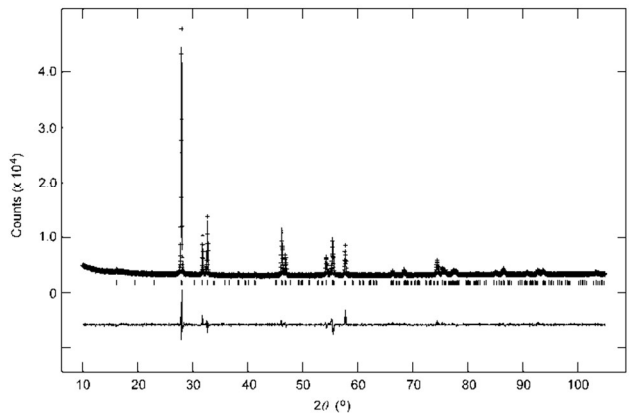

Fig. 2. Fitted diffraction profiles for $Bi_{14}YO_{22.5}$ at room temperature showing observed (+ signs) calculated (line) and difference (lower) profiles. Reflection positions are indicated by markers; (a) neutron back-scattering, (b) neutron low-angle and (c) X-ray fits are shown.

RSC Advances Accepted Manuscript

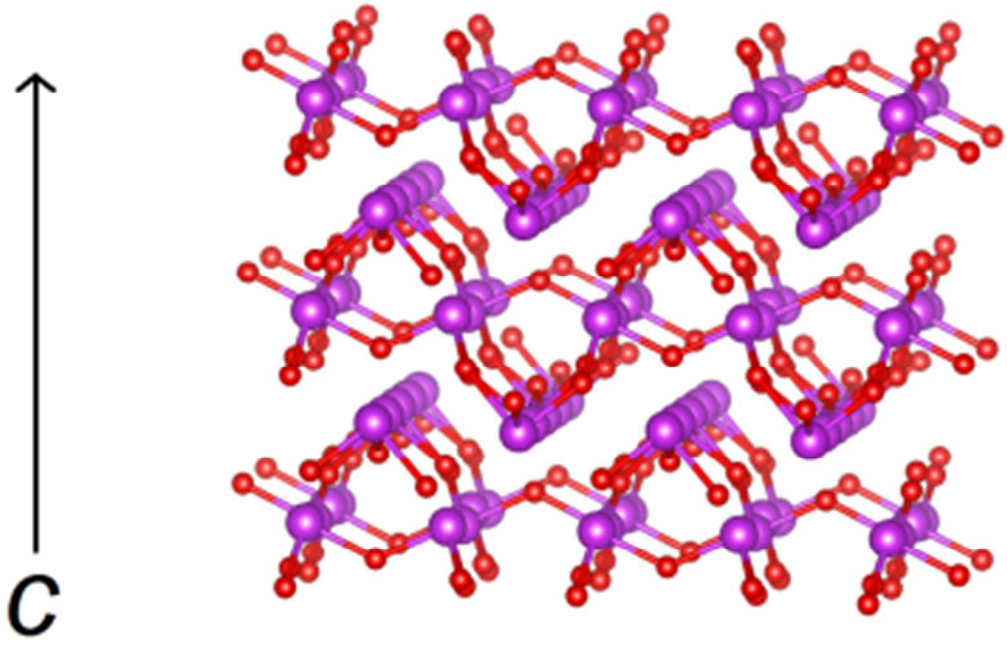

Fig. 3. Idealised structure of β_{III}-$Bi_{14}YO_{22.5}$ (excluding disorder for clarity) showing corrugated layers of bismuth oxide. Cations are indicated by violet spheres and oxide ions by red spheres. The *c*-axis direction is indicated.

RSC Advances Accepted Manuscript

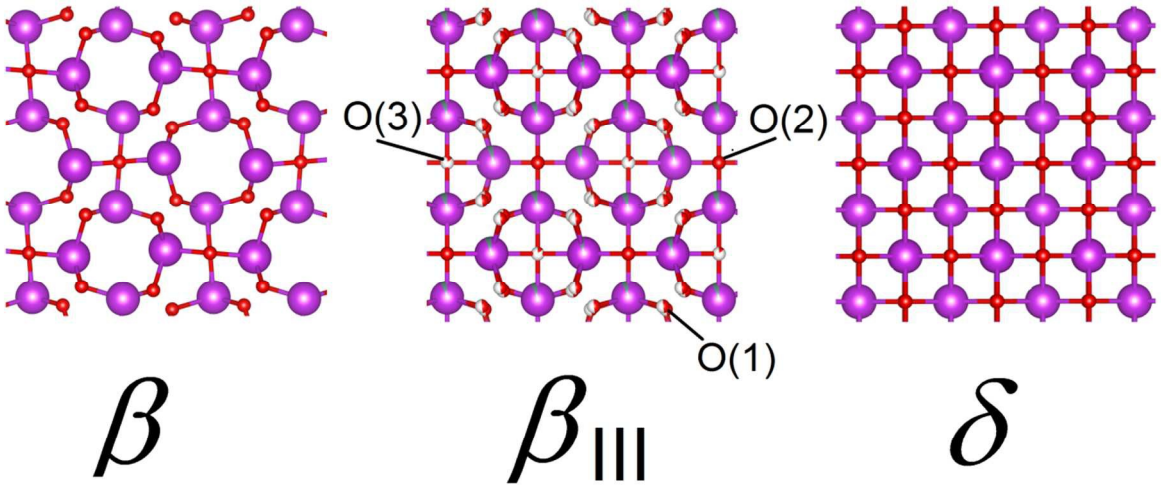

Fig.4. Comparison of structures for β-Bi_2O_3, β_{III}-$Bi_{14}YO_{22.5}$ and idealized structure of δ-Bi_2O_3. Cations are indicated by violet spheres, with oxide ions by red spheres and disorder indicated by partial filling of spheres.

RSC Advances Accepted Manuscript

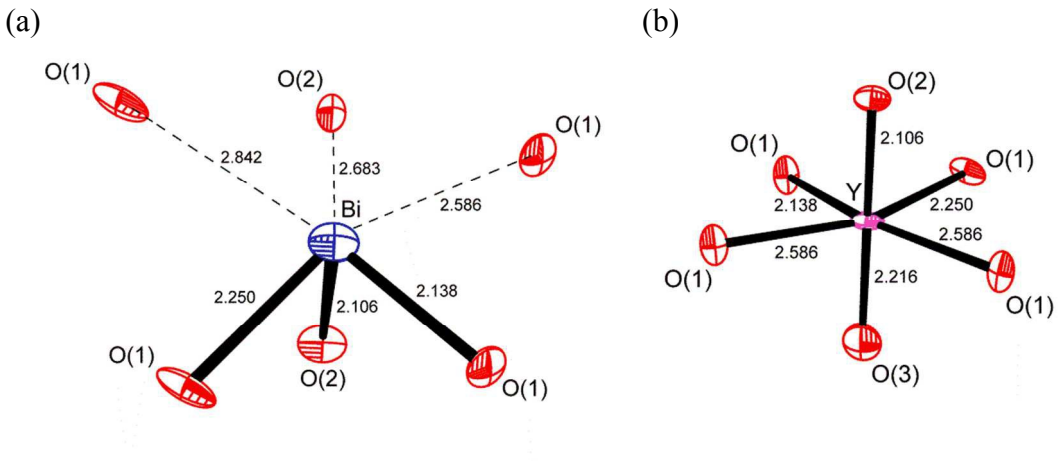

Fig. 5. Proposed coordination geometries for (a) bismuth atoms; (b) yttrium atoms. Contact distances (Å) are shown with non-bonding interactions indicated by dashed lines. Thermal ellipsoids are drawn at 50% probability.

RSC Advances Accepted Manuscript

(a) (b)

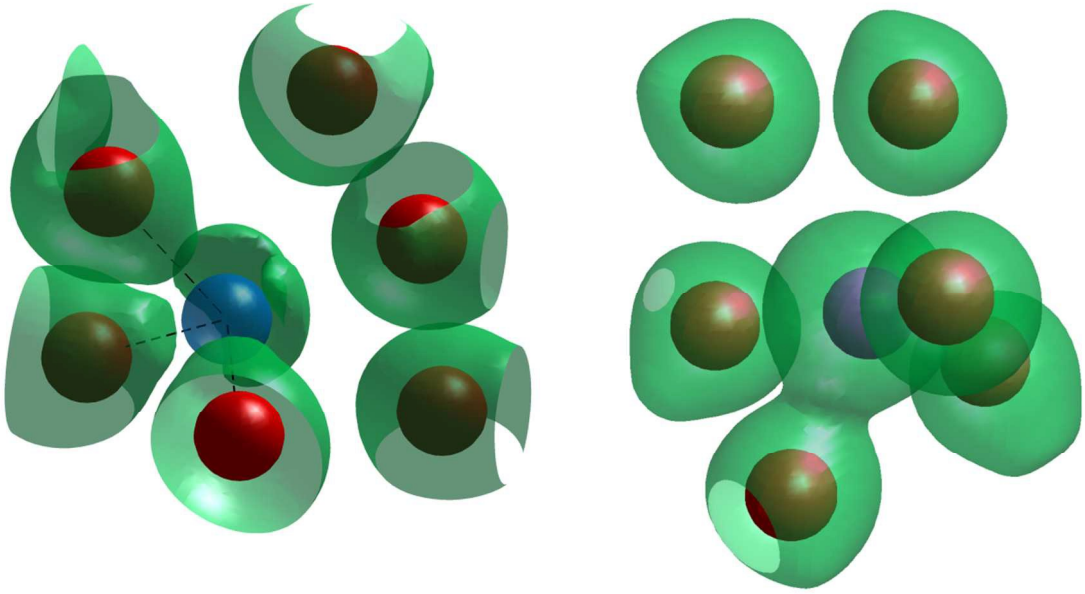

Fig. 6. Iso-surface plots of valence electron density from *ab initio* calculation of β_{III}-$Bi_{14}YO_{22.5}$ showing (a) bismuth environment and (b) yttrium environment. Positions of bismuth, yttrium and oxygen atoms are indicated by blue, violet and red spheres, respectively.

RSC Advances Accepted Manuscript

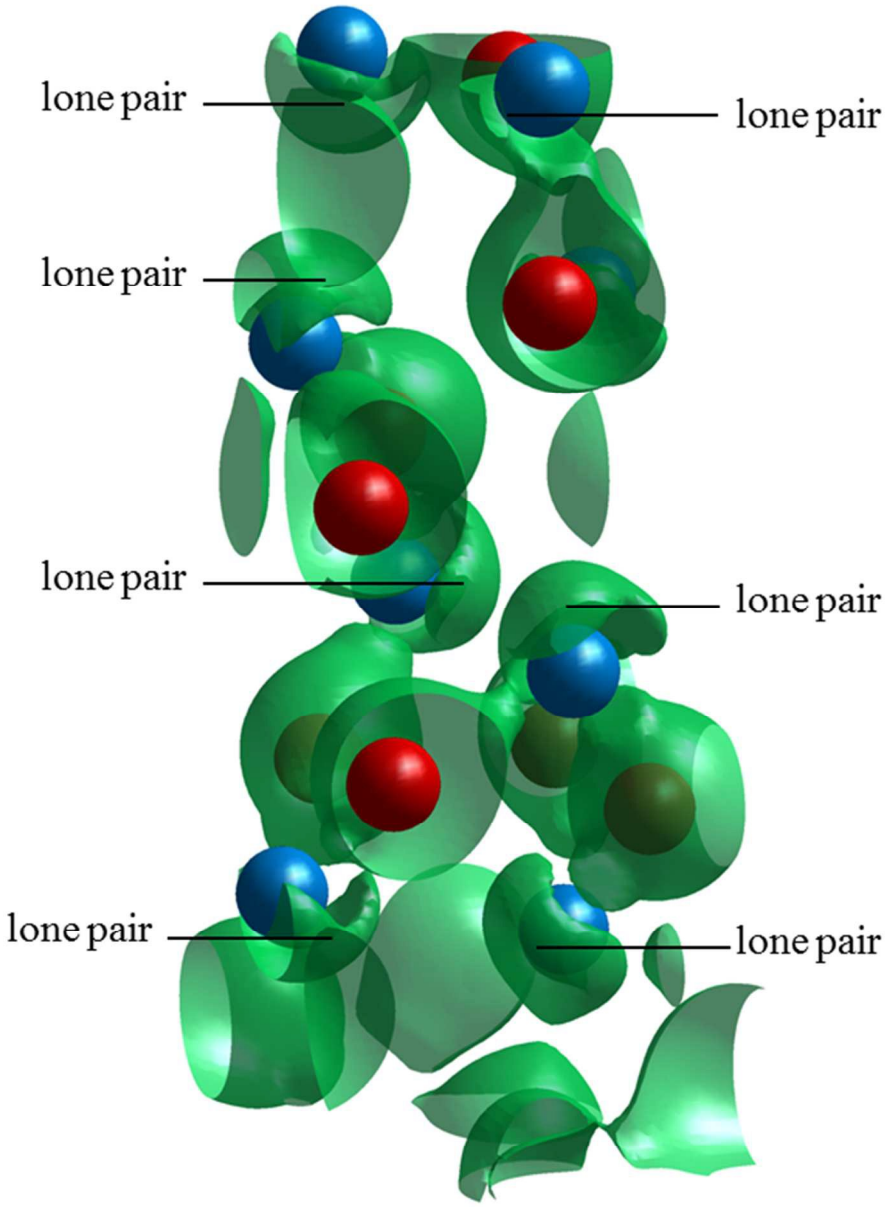

Fig. 7. Iso-surface plot derived from *ab initio* calculations showing valence electron density around vacant channel in β_{III}-$Bi_{14}YO_{22.5}$. Positions of bismuth and oxygen atoms are indicated by blue and red spheres, respectively. The bismuth lone electron pairs are marked.

RSC Advances Accepted Manuscript

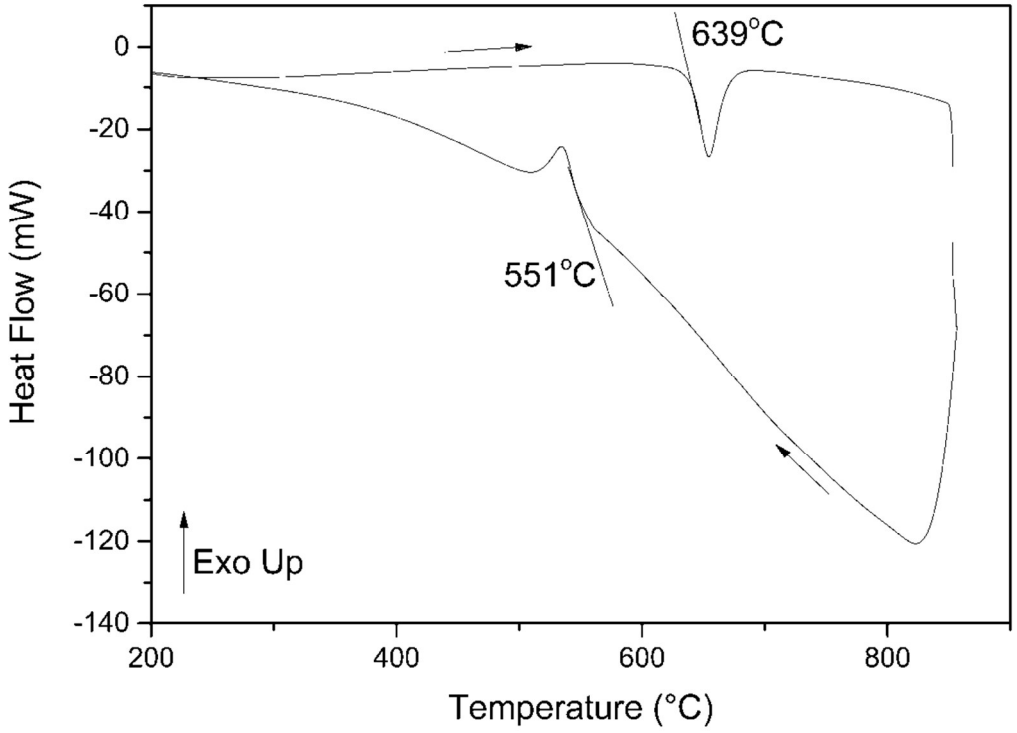

Fig. 8. DTA Thermogram for $Bi_{14}YO_{22.5}$. Heating and cooling runs are indicated by arrows.

RSC Advances Accepted Manuscript

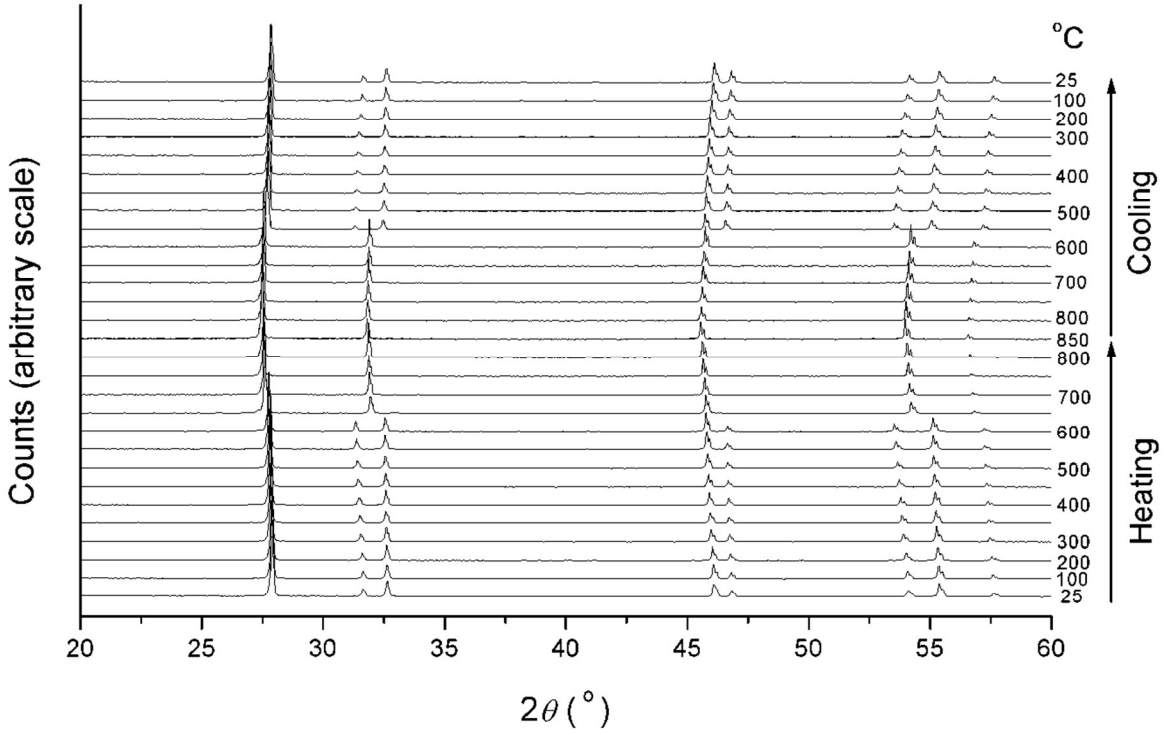

Fig. 9. X-ray diffraction patterns for $Bi_{14}YO_{22.5}$ on heating and cooling.

RSC Advances Accepted Manuscript

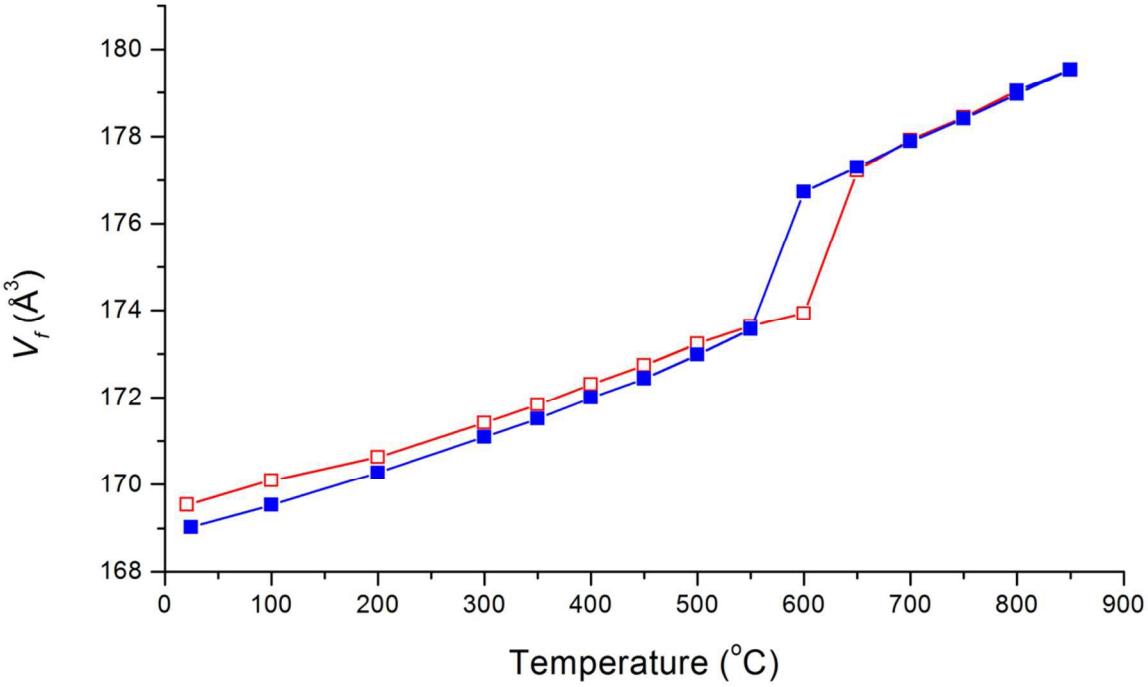

Fig. 10. Thermal evolution of equivalent fluorite volume, V_f, in $Bi_{14}YO_{22.5}$ on heating (open symbols) and cooling (filled symbols).

RSC Advances Accepted Manuscript

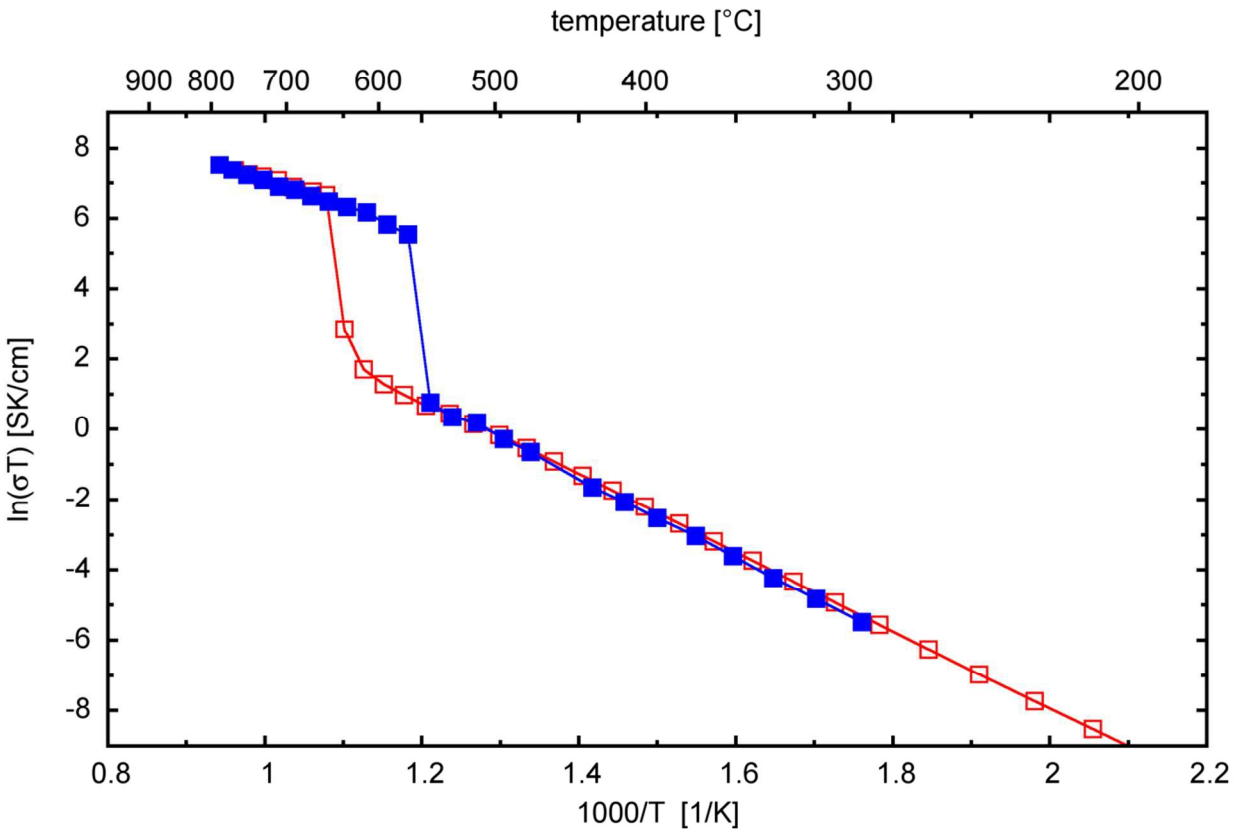

Fig. 11. Arrhenius plot of total electrical conductivity for $Bi_{14}YO_{22.5}$ on successive heating (open symbols) and cooling (closed symbols) runs.

RSC Advances Accepted Manuscript

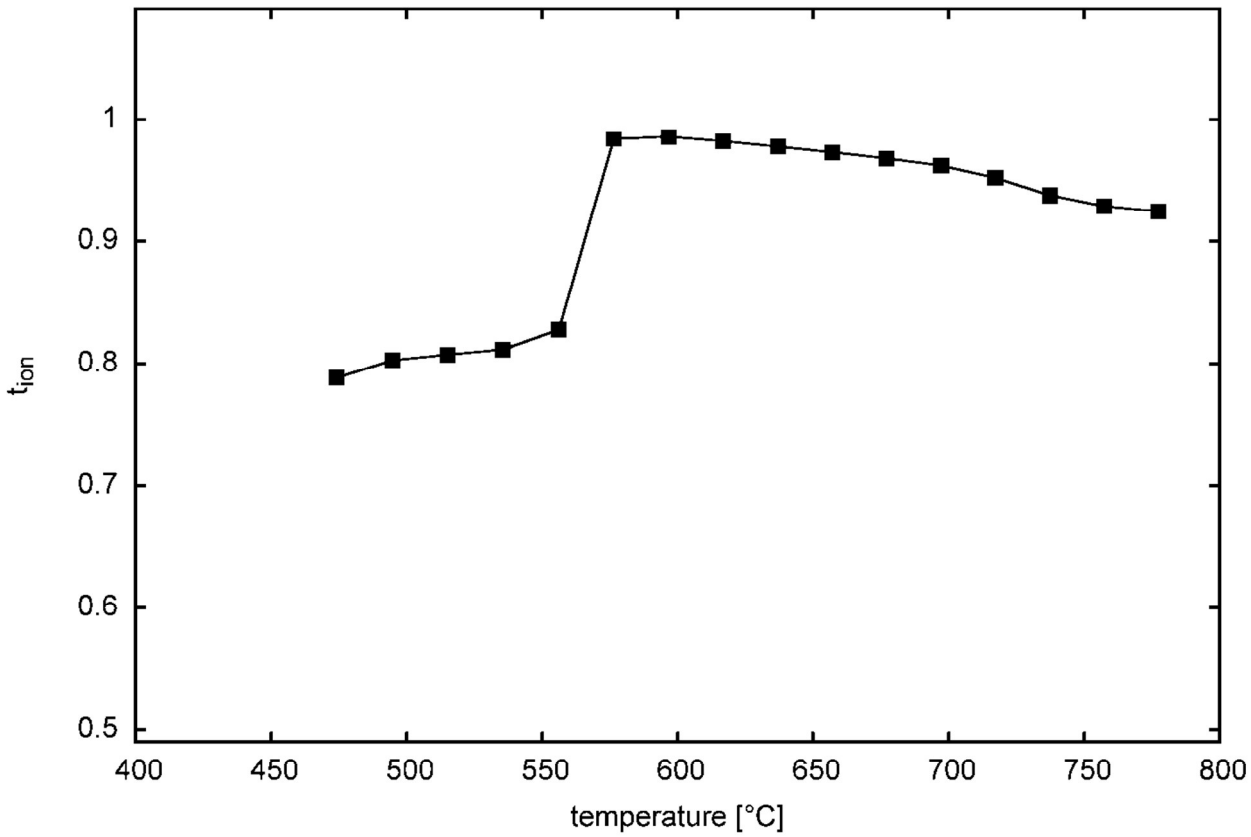

Fig. 12. Thermal variation of ionic transference number in $Bi_{14}YO_{22.5}$

RSC Advances Accepted Manuscript

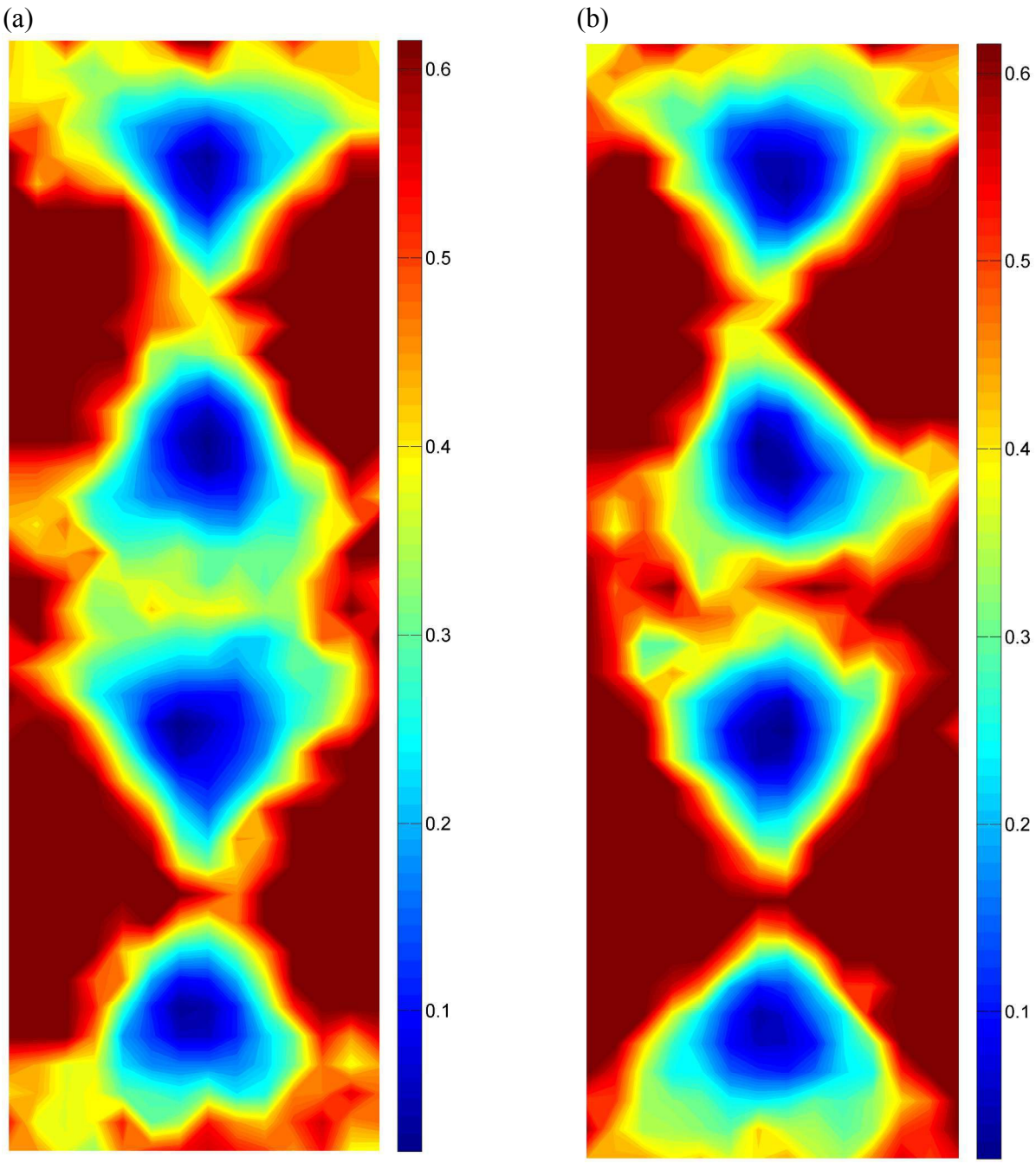

Fig. 13. Energy distribution landscapes in β_{III}-$Bi_{14}YO_{22.5}$, showing sections through (a) an empty channel and (b) a filled channel. Scales are given in eV

RSC Advances Accepted Manuscript

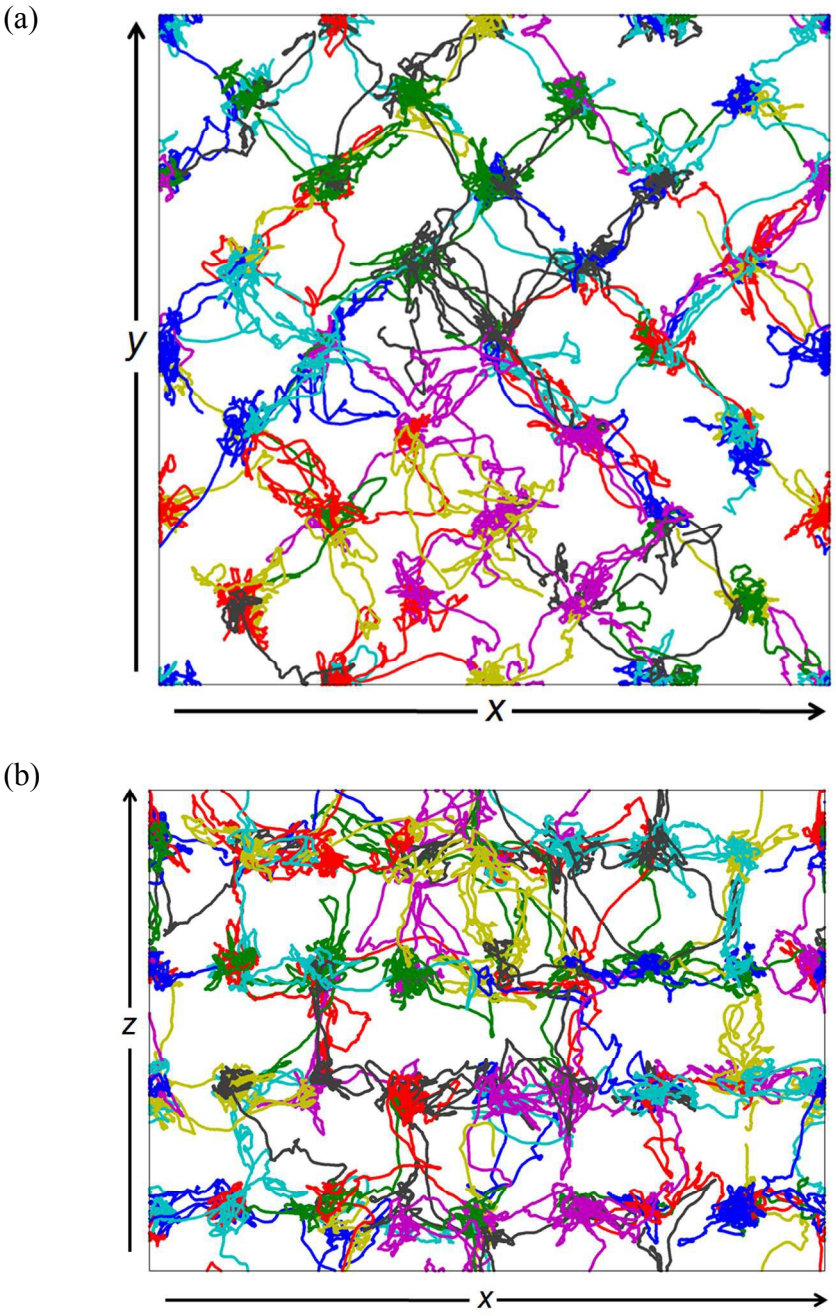

Fig. 14. Individual oxide ion trajectories (marked by different colours) projected onto (a) *x*-*y* and (b) *x*-*z* planes in β_{III}-$Bi_{14}YO_{22.5}$.

RSC Advances Accepted Manuscript

Table of contents entry

Ab initio molecular dynamics calculations show low energy barriers for oxide ion conduction along *c*-axis channels in β_{III}- $Bi_{14}YO_{22.5}$

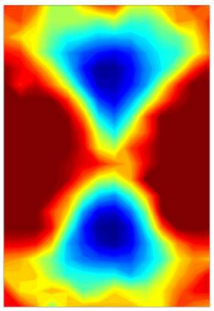

RSC Advances Accepted Manuscript